

Adaptive Clutter Rejection Filtering in Ultrasonic Strain-Flow Imaging

Christian Kargel, *Associate Member, IEEE*, Gernot Höbenreich, Birgit Trummer, and Michael F. Insana, *Member, IEEE*

Abstract—This paper introduces strain-flow imaging as a potential new technique for investigating vascular dynamics and tumor biology. The deformation of tissues surrounding pulsatile vessels and the velocity of fluid in the vessel are estimated from the same data set. The success of the approach depends on the performance of a digital filter that must separate echo signal components caused by flow from tissue motion components that vary spatially and temporally. Eigenfilters, which are an important tool for naturally separating signal components adaptively throughout the image, perform very well for this task. The method is examined using two tissue-mimicking flow phantoms that provide stationary and moving clutter associated with pulsatile flow.

I. INTRODUCTION

CLUTTER suppression in ultrasonic color-flow (CF) imaging is a challenging signal processing problem. The goal is to isolate signals from flowing blood that are summed with clutter signals, i.e., echoes from stationary or slowly moving extravascular scatterers. At ultrasonic frequencies below 20 MHz, the scattering amplitude from tissue echoes is orders of magnitude greater than that from red blood cells (RBCs), so CF imaging is often dominated by clutter signals that produce, for example, flash artifacts. Even if the sample volume¹ is entirely contained within a blood vessel, reverberations can bias velocity estimates significantly. Under slow-flow conditions, as in tumor imaging, the blood and clutter echoes often share the same Doppler frequency bands, thus increasing the challenge to separate signals.

Usually clutter signals are discarded as a nuisance. However, clutter signals convey information about the displacement and elasticity of tissues surrounding the vessel lumen [1]. Spatial derivatives of displacement yield strain estimates that describe tissue [2], [3] or vascular [4], [5] elasticity via strain imaging. This paper focuses on filtering techniques that are able to separate the blood and tissue components of motion to simultaneously image tissue strain and blood flow from the same set of echo data.

Manuscript received August 21, 2002; accepted February 3, 2003. This study was supported by NIH CA82497.

Ch. Kargel is with the Department of Medical Information Technology at the Carinthia Tech. Institute, University of Applied Sciences, Austria (e-mail: c.kargel@cti.ac.at).

G. Höbenreich, B. Trummer, and M. F. Insana are with the Department of Biomedical Engineering, University of California, Davis (e-mail: mfinsana@ucdavis.edu).

¹The sample volume is the volume of the scattering medium that contributes to the echo signal for any one velocity estimate. It is determined by pulse volume and range gate properties.

Highpass (HP) digital filtering of pulsed Doppler signals is most effective for suppressing clutter if the RBC velocity is much higher than the tissue velocity, and the respective Doppler spectra are nonoverlapping. The degree of spectral separation determines the specification for classical HP filter design in terms of filter characteristics, order, corner frequency, and ripple. A narrow separation demands high order filters to provide a narrow transition band. Infinite impulse response (IIR) filters are superior to finite-impulse response (FIR) filters under these conditions, but high order IIR filters yield significant transient responses and thus require longer settling times. Unfortunately, the number of samples per line-of-sight (LOS), or packet size N , must be kept small ($2 \leq N \leq 20$) to achieve real-time CF frame rates. The IIR filter initialization techniques are known to reduce transient filter responses [6], [7]. Another approach is to apply regression filters that treat input samples as polynomial functions in the time domain and perform least-square regression analysis [8].

The complexity of filter design increases considerably when clutter and blood spectra overlap. This is often the case for tumor imaging where the RBC velocity is relatively slow and spatially disorganized, thus producing low mean-frequency Doppler spectra in the clutter band. Neovascularization is accompanied by a collagenous structural remodelling of the parenchymal tissues that stiffens the tumor and adjacent regions as they become fibrotic [9] and desmoplastic [10]. Combined strain-flow (SF) imaging may improve our understanding of tumor development and their responses to the new classes of antiangiogenic therapies [11].

To measure blood velocity and tissue elasticity simultaneously, we developed a laboratory ultrasound scanner capable of standard and novel procedures for tumor imaging [12], [13]. Specifications for clutter filter design are unique and best implemented using an adaptive approach. The performances of adaptive clutter filters for CF imaging were evaluated recently by Bjærum *et al.* [14] for data acquired while moving the probe in search of small blood vessels. Their investigation included a) signal down-mixing with a temporally and spatially averaged estimate of the mean Doppler frequency, b) down-mixing with varying phase increments to adapt to accelerated tissue motion, c) eigenvector-based regression filters, which, for first-order filters, turn out to be approximately equal to b), and d) prewhitening of clutter and noise spectra prior to velocity estimation. The authors concluded that method b) provides the best performance if evaluated with power

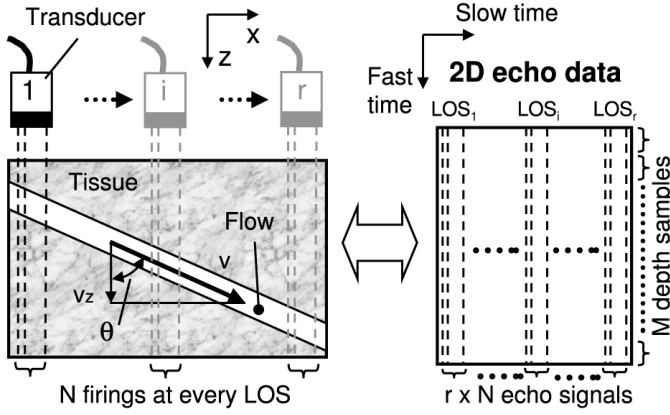


Fig. 1. Scan-mode acquisition for CF imaging (left) and matrix representation of data (right). Matrix dimensions are $M \times rN$. The situation for M-mode is similar except there is no transducer motion along the x -axis ($r = 1$), and only a single LOS is investigated as a function of time.

Doppler. However, we felt the tremendous computational load of b) warrants further investigation of the second best filter method c). In our application, basis functions for the clutter space are created to adapt to specific realizations of clutter signal statistics. Probe movement in the Bjærum study produced a uniform velocity over the entire region-of-interest (ROI) at any instant of time. Our task is different—we hope to separate spectra in a SF imaging environment in which the clutter varies temporally and spatially.

II. FLOW VELOCITY ESTIMATION

To measure low blood velocities with high accuracy, precision and reasonably high frame rates, we used the 2-D autocorrelation estimator [15]. This estimator combines the 1-D Kasai autocorrelator [16], commonly used in CF imaging, with mean radio frequency estimation for the compensation of frequency-dependent attenuation and scattering. Compared to the Kasai autocorrelator, the 2-D autocorrelator yields significantly lower estimation bias and variance with only a moderate increase in computation load [13].

Digitized echo signals are organized in 2-D arrays where the terms “fast-time” (columns) and “slow-time” (rows) define the direction of the beam axis (echo signal sampling rate f_s , index m) and pulse packet dimension (pulse repetition sampling rate f_{PRF} , index n), respectively. The column index in the CF image is r . This data structure is depicted in Fig. 1.² Provided that scatterers move at velocity \mathbf{v} , the mean Doppler frequency computed from slow-time samples is $f_D = 2v_z f_0 / c$ where $v_z = |\mathbf{v}| \cos \theta$ is the axial velocity component, θ is the Doppler angle (between beam axis and velocity vector \mathbf{v}), f_0 is the signal radio-frequency and c is the longitudinal sound speed. v_z can be estimated using the complex 2-D correlation func-

tion $R(k, \ell)$ at lags $(k, \ell) = (0, 1)$ and $(k, \ell) = (1, 0)$ [15]

$$v_z = \frac{c}{2} \frac{f_{PRF} \angle \hat{R}(0, 1)}{2\pi f_{dem} + f_s \angle \hat{R}(1, 0)}, \quad (1)$$

where f_{dem} is the demodulation frequency used for coherent quadrature demodulation and \angle represents phase angle. \hat{R} is an estimate of the complex 2-D correlation function computed from complex baseband signals $I(m, n) + jQ(m, n)$ recorded in the range gate at a certain LOS

$$\hat{R}(k, \ell) = \sum_{m=0}^{M'-k-1} \sum_{n=0}^{N-\ell-1} [I(m, n) + jQ(m, n)] \cdot [I(m+k, n+\ell) - jQ(m+k, n+\ell)], \quad (2)$$

where $M' \leq M$ is the number of axial echo samples in the range gate. The velocities estimated from the autocorrelation function are unbiased for symmetric Doppler power spectra. With additive white Gaussian noise (WGN), this also holds true in the limit of infinite packet size [17]. Detailed error analysis of autocorrelation-based velocity estimators for CF imaging is described in [13].

Properly designed fast-time RF filters maximize the SNR and allow accurate measurements of the mean frequency of the RF signals in noise. To achieve this objective, the amplitude response of the RF filter in the band-pass must be flat or, at minimum, symmetric about the true mean to prevent noise from biasing the mean RF frequency estimates.

III. STRAIN ESTIMATION

Strain images are usually formed from crosscorrelation-based displacement estimates. Local displacements are usually determined from pairs of RF data frames acquired for the same region in the object but at two different times, representing different stages of deformation. Like B-mode and unlike CF imaging, strain images employ high bandwidth pulse transmission and $N = 1$. The Chaturvedi algorithm [3] was applied to estimate displacement and image strain. The algorithm was originally developed for imaging strain resulting from external compression but has been applied to vascular imaging of internal deformation [5].

Strain is nonzero when the local displacements vary with position in the scan plane. The algorithm is designed to measure local displacements within the deformed object from 1-D or 2-D correlation lags determined at three spatial scales. First, the coarsest estimates of displacement are used to measure the overall displacement and average strain in the plane applied to one frame with respect to another. The echo data in a frame are then warped in two dimensions to compensate for the average physical deformation using a process known as global companding. Second, 2-D displacements measured at an intermediate-size spatial resolution are recorded and used to warp the echo fields via a local companding process. Finally, displacements are measured at the highest spatial resolution

²Although Figs. 1–11 are placed near the associated text, Figs. 12–16 are placed on a single color page.

by 1-D axial correlation of twice companded echo frames. Displacements measured at each stage of the process improve the condition of the data for displacement estimation at higher resolution [18]. Finally, the summed components of displacement along the ultrasonic beam axis measured at each stage are filtered by a simple first-order linear FIR differentiator to form strain images. Axial strain pixel size is determined by sampling rate and correlation parameters. These parameters and the impulse response of the instrumentation combine to determine the spatial resolution of the strain image.

The above procedure was designed for quasi-static strain imaging using external compression. To image internal deformation from pulsed flow, global companding is unnecessary for phantoms but applied when scanning *in vivo* to compensate for in-plane transducer motion common with hand-held scanning devices. The flexibility of our laboratory imaging system allows the application of various ultrasonic pulsing strategies useful for imaging internal deformation. For example, the rising edge of the cardiac pulse rapidly expands the lumen of normal brachial arteries by hundreds of microns in just a few milliseconds. Frame rates lower than 30/s result in echo decorrelation near the vessel wall where the displacement is greatest. We can increase the pulse-repetition frequency (PRF) in our lab system and apply multiple broadband pulses at a given LOS, similar to packets for CF imaging and the elasticity imaging methods of Nightingale *et al.* [19], to detect rapid local movements. Furthermore, accurate positioning of the transducer (better than 100 nm) together with appropriate gating techniques allow data acquisition from 2-D regions for repetitive physiological signals (see Fig. 13 and 14). Two-dimensional local companding is not possible for M-mode data. Fortunately, when the PRF is sufficiently high, tissue movement between pulse transmissions is small enough to be estimated using 1-D cross-correlation methods without significant decorrelation. Adding individual interpulse displacements gives the net displacement. To achieve unbiased subsample displacement estimates, we chose $\sin x/x$ interpolation of the cross-correlation function for best possible results over less accurate alternative interpolation techniques [20], [21]. To maximize numerical efficiency, cross-correlation and interpolation were both implemented in the Fourier domain.

IV. SF IMAGING

The ultrasonic pulsing requirements for imaging strain and flow individually are often not the same. Generally, CF imaging requires large packet sizes and narrow-band pulses to minimize velocity errors in larger vessels with steady flow conditions. Conversely, strain imaging usually employs a packet $N = 1$, two or more frames of RF data, and broadband pulses. Shorter pulses help to minimize the amount of tissue deformation that occurs on the scale of the pulse volume and in turn minimize severe strain noise from signal decorrelation. If the conditions include pulsatile flow in small vessels or high flow gradients, then

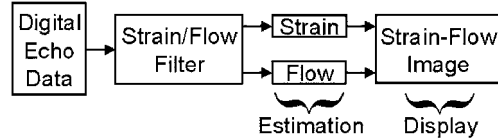


Fig. 2. Block diagram of combined strain-flow imaging.

short-duration wide-bandwidth pulses and smaller packet sizes are selected. Consequently, the pulsing requirements for the two methods can converge in some challenging situations, such as tumor imaging. In this study, we chose one pulse bandwidth that minimized strain-flow estimation errors for specific imaging situations in phantoms. For critical applications in which the highest performance is required for both strain and flow, pulse interleaving techniques can be applied.

The SF imaging performance, measured in terms of velocity and strain errors or imaging detectability, also depends on the effective separation of tissue and blood motion components in the echo signal. Fortunately, the two components can be largely complementary, e.g., when tissue motion is responsible for most of the clutter signal. An HP clutter filter effective for CF imaging provides the design for how to filter for strain. The output of the filter complement represents the necessary lowpass filtering for strain imaging. A block diagram of a combined SF imaging system is shown in Fig. 2. If the SF filter is well-designed for the conditions, vessel regions in the strain image will be filled completely with decorrelation noise, and all of the CF signal will be located in vessels. However, if the clutter signal also includes nonphysiological motion, e.g., transducer motion, then two parallel filters must be designed to isolate the two principal motion components. Individual filters are also necessary when the quality of the filter complement signal is insufficient for strain estimation. For example, a Chebyshev type II HP filter (equal amplitude ripples in the stopband) is a simple and effective choice for velocity estimation [21]. However, strain estimation using the filter complement can be very much influenced by the filter response ripples, which for clutter signals appear in the passband. We will show that the quality of strain estimates in SF imaging can be significantly improved by applying an adaptive clutter rejection filter optimized for CF imaging. In the next section, basic properties of various filter classes appropriate for CF imaging are briefly reviewed.

V. CLUTTER FILTER DESIGNS

Displacement estimates are essentially phase measurements. Therefore, phase distortions introduced by a clutter filter add errors to both velocity and strain images when using the entire pulse packets for combined strain-flow measurements. The FIR filters and zero-initialized IIR filters are linear time-invariant (LTI) systems and consequently introduce no estimation bias from phase distortion.

To see why this is true, assume an echo-signal input sequence $x[n]$ that is a wide-sense stationary (WSS) discrete-time complex random process with autocorrelation function $R_x[n]$. This input is applied to an LTI filter with impulse response $h[n]$. The output is given by the convolution $y[n] = h[n] * x[n]$, and the relation between input and output autocorrelation functions is

$$R_y[n] = h[n] * h^*[-n] * R_x[n], \quad (3)$$

where $[\dots]^*$ denotes complex conjugation. The discrete-time Fourier transform of (3) gives the corresponding power spectral densities, [21] $S_y(e^{j\omega}) = |H(e^{j\omega})|^2 S_x(e^{j\omega})$, where the mean Doppler frequency is proportional to velocity. However, (3) is not valid for commonly used initialized filters because they are non-LTI systems; e.g., the step-initialized IIR filter is nonlinear because the output can be nonzero for times larger than t_0 even if the input was zero for all times prior to t_0 [21]. While non-LTI filters have many advantages, the distortion of the complex autocorrelation phases should be considered when using autocorrelation-based estimation techniques.

The filter amplitude response is also important for velocity estimation. In noise-free Doppler spectra in which the blood flow and clutter components do not overlap in frequency, biased velocity estimates will result if the pass-band amplitude response is not flat. Additive WGN does not bias autocorrelation-based velocity estimates because its autocorrelation is zero at all lags different from zero. However, this desirable feature fails when clutter rejection filtering is applied, even for LTI filters.

Filter impulse and frequency responses are defined once the transient responses have completely settled. Such conditions are difficult or impossible to achieve when small packet sizes are used, which is why we need an alternative method for characterizing the filter performance in CF imaging. Torp [22] characterized these filter responses from the ratio of output-to-input signal power when the input is a complex exponential. The power of a complex sinusoid is constant and independent from the phase of the input signal, which, of course, is not the case for real-valued sinusoids. We have adopted this definition of the clutter filter frequency response as applied to complex baseband IQ signals. Power-ratio measurements can be swept in frequency to map the filter attenuation. Group delay cannot be defined in the traditional sense for many of these filters.

A. FIR Filters

Given that N is small for real-time applications, low-order FIR filters are inappropriate for CF imaging because the transition frequency band is often too large. Furthermore, the number of valid output samples, viz., N minus the filter order, becomes too small when one considers that the variance for autocorrelation estimates is inversely related to the number of valid filter output samples. While we do not consider FIR designs, it has been shown that minimum-phase FIR filters and mirroring techniques can yield acceptable performance [23].

B. IIR Filters

The IIR filters exhibit narrower transition bands than FIR filters for the same order. However, appropriate initialization of the internal filter states must be applied in order to suppress the transient filter response. Three different initialization techniques are investigated in this paper [7]:

- Zero initialization: the initial filter state vector is set to zero for times less than zero. Often, this technique yields unacceptably large transients, although this filter is LTI, and therefore its phase response does not influence autocorrelation-based velocity estimation.
- Step initialization: the filter state vector is set to a constant determined by filter coefficients and data values. Transients can be partially suppressed from *a priori* knowledge that the input signal is dominated by high-amplitude, very low Doppler-frequency (stationary) clutter. We apply a unit-step input and calculate the internal filter states at $t = \infty$. These values are scaled at each range depth (fast-time) by the amplitude of the first data sample in the pulse packet before being loaded into the filter.
- Projection initialization: the filtered signal is decomposed into steady-state and transient components. Using an appropriate projection operator [7], which projects the signal in the “transient response subspace,” it is possible to decompose the filtered signal into two orthogonal components and subtract the transient subspace component from the output.

C. Polynomial Regression Filters

Regression filters operate on the assumption that the slowly varying clutter component in the signal can be approximated by a polynomial. The least-squares fit to this low-frequency clutter component in the echo signal is subtracted. The curve set can be chosen to form an orthonormal basis for a K -dimensional clutter subspace of the N -dimensional signal space. The least-squares clutter fit is the projection of the signal into the clutter subspace. The linear filtering operation can be generally expressed as

$$\mathbf{y} = \mathbf{A}\mathbf{x}, \quad (4)$$

where \mathbf{x} is the complex input signal vector (slow-time samples), \mathbf{y} is the complex output vector, both of dimension $N \times 1$, and \mathbf{A} is an $N \times N$ dimensional filter matrix,

$$\mathbf{A} = \mathbf{I} - \sum_{k=1}^K \mathbf{b}_k \mathbf{b}_k^H. \quad (5)$$

\mathbf{b}_k is the set of basis vectors, for orthonormal bases often Legendre or Chebyshev polynomials, $(\dots)^H$ is the Hermitian operator, and \mathbf{I} is the identity matrix. The frequency response of the filter can be calculated by

$$H(e^{j\omega}) = 1 - \frac{1}{N} \sum_{k=1}^K |B_k(e^{j\omega})|^2, \quad (6)$$

where $B_k(e^{j\omega})$ is the discrete-time Fourier transform of the basis vector \mathbf{b}_k [22]. In order to design HP filters, K must be small. Regression filters are adaptive in the sense that the polynomial coefficients vary depending on the data.

D. Eigenfilters

The eigenfilter approach is to create a unique set of basis functions for a specific clutter space that adapts to the statistics of that clutter signal. Since the entire basis set and not only scaling coefficients are determined from the data, eigenfilters are truly adaptive. The Hotelling transform³ decomposes the data vector \mathbf{x} into N eigenvectors $(\mathbf{e}_1, \dots, \mathbf{e}_N)$ of the clutter covariance matrix \mathbf{C}_C ⁴

$$\mathbf{C}_C = \mathcal{E}\{\mathbf{x}\mathbf{x}^H\}, \quad (7)$$

where $\mathcal{E}\{\cdot\}$ is the expected value. In the common situation where echo-signal energy from clutter is much greater than that from blood flow, the largest eigenvalues correspond to the clutter component. The Hotelling transform decomposes the echo signal into an orthogonal basis set. These basis functions are then arranged in descending order of energy. Clutter and noise can be suppressed by removing certain eigencomponents. First-order eigenfilters ($K = 1$) are implemented by subtracting the eigencomponent with the highest energy from the input signal. Second-order eigenfilters ($K = 2$) subtract the highest and second highest energy components. While clutter is usually contained in a subspace defined by $(\mathbf{e}_1, \dots, \mathbf{e}_K)$ with $K < N$, white noise is spread over all eigencomponents. All subspace eigencomponents that do not contain blood flow can be subtracted to increase the overall SNR.

Eq. (5) and (6) are used to calculate the filter matrix \mathbf{A} and filter frequency response. In practice, \mathbf{C}_C is unknown *a priori* but can be estimated from the data by spatial averaging:

$$\hat{\mathbf{C}}_C = \frac{1}{M'} \sum_{i=1}^{M'} \mathbf{x}_i \mathbf{x}_i^H. \quad (8)$$

The specificity of the filter to a particular data set with clutter is maximized by choosing a region in the data that excludes any blood flow. That region can be selected automatically by locating the subregion of data that exhibits maximum slow-time echo coherence by means of thresholding the velocity spread or choosing the first eigencomponent. It is unnecessary to assume temporal stationarity in slow-time when computing the correlation matrix, and therefore, the eigenfilter is able to adapt to clutter from

³Hotelling was the first to derive the transformation of discrete variables into uncorrelated coefficients. He referred to it as the "method of principal components." The analogous transformation for transforming continuous data was discovered by Karhunen and Loève [24].

⁴Clutter signals are assumed to stem from a zero-mean complex Gaussian random process. Hence the covariance and correlation matrices are equal.

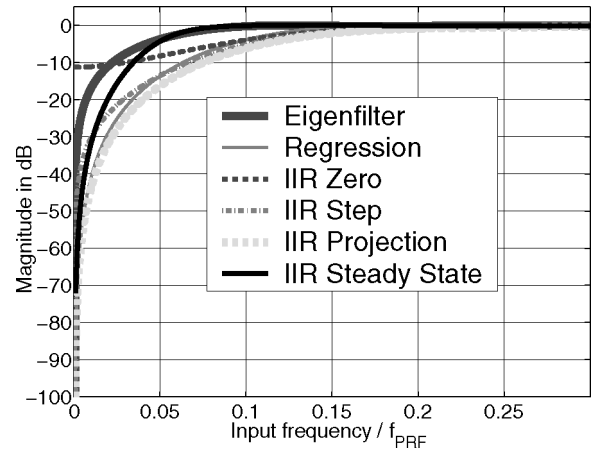


Fig. 3. Frequency responses of HP filters ($N = 8$). The maximum (aliasing) frequency is $0.5 f_{\text{PRF}}$ (not shown). Second-order IIR Chebyshev filters were designed with a cut-off frequency of $0.0566 f_{\text{PRF}}$ Hz to match the -3 dB point of the eigenfilter designed for stationary clutter signals (zero Doppler shift).

accelerated tissue [14]. However, wide sense stationarity in fast-time is necessary for the estimation of $\hat{\mathbf{C}}_C$, and the depth region for averaging must be chosen appropriately.

E. Comparison of the Filter Frequency Responses

Fig. 3 shows the frequency responses of the different HP filters described above and for a packet size $N = 8$. Initialization of second-order IIR filters with Chebyshev characteristics largely suppresses transients and thereby improves the frequency response. For comparison, we also show the steady-state response, which cannot be achieved in CF imaging due to the small N . The zero-initialized IIR filter provides a zero-frequency attenuation of only 11 dB, which is inadequate for CF imaging. The projection-initialized IIR filter and the first-order regression filter have generally similar frequency responses. For the parameters here, the step-initialized IIR filter also has similar performance. The frequency response of the first-order ($K = 1$) eigenfilter is closest to the second-order steady-state IIR filter. A more detailed study of filter performance as a function of various parameters can be found in [25].

F. Summary of Design Considerations

The traditional approach to highpass digital filter design is to select a filter type, corner frequency, transition band, error tolerances, and frame rate and then compute the minimum filter order. Provided that $N < 8$, our experience shows that second-order IIR filters provide a reliable compromise in phantom studies. If the clutter is from stationary scatterers and the echo SNR is high, a step-initialization IIR filter provides sufficient performance at low computational load. It adapts to the data by finding a single initial filter value. If the clutter is from moving scatterers and varies spatially, we increase the degrees of freedom for motion (and complexity) by choosing a projection-initialized IIR filter, regression filter, or eigenfilter depend-

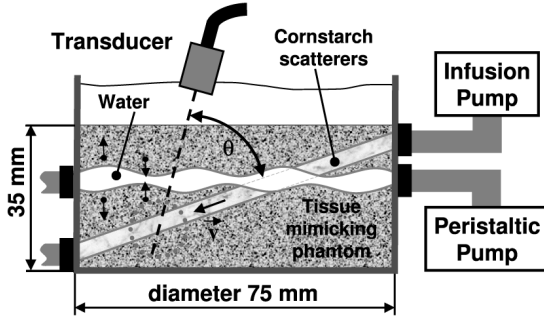


Fig. 4. Phantom experiment for generating clutter. Echo data were acquired in M-mode in the vicinity of the circled region.

ing on tissue acceleration, echo SNR, and required CF frame rate. The most complex imaging environments require maximum filter adaptability, which is provided by the eigenfilter at the cost of the greatest computational load. In such situations eigenfilter parameters must adapt to spatial changes in the clutter component of tissue scattering. Yet, there must also be a subset of the data set acquired for each frame that can be considered wide sense stationary in fast-time to allow averaging when determining filter basis functions. Because physiological displacements from cardiac pulses are small compared with RBC displacements, we often average data over all M depth samples to compute eigenvectors and therefore filter properties. Averaging over a much larger depth than the speckle correlation length is necessary to obtain a good estimate of the clutter covariance matrix. We assume the echo data are spatially stationary over the M samples. If that is not the case, the M -sample waveform must be subdivided into segments of duration M' that are WSS. Consequently, prior knowledge of the ROI can help with the adaptation of the filter to specific imaging conditions.

VI. RESULTS AND DISCUSSION

A. Phantom Experiments

The performance of clutter rejection filters applied to strain-flow imaging was examined with the experiment diagrammed in Fig. 4. Two phantoms with this geometry were designed. First, a *solid* tissue-mimicking graphite-gelatin phantom was constructed with two wall-less cylindrical flow channels [5]. A low gelatin concentration produced a soft material ($c = 1561 \pm 1$ m/s, elastic modulus 18 kPa, [26]), while the graphite concentration was adjusted to give ultrasonic absorption and backscatter that is tissue-like [27]. A 3-mm-diameter channel with circular cross section was connected to an infusion pump that generated steady Poiseuille flow for CF imaging. The maximum velocity within the parabolic flow profile was approximately 17 mm/s. The scattering fluid in the channel was a sparse (1% by mass) suspension of cornstarch in water. Before use, the suspension was heated to 100°C

for several minutes and cooled to room temperature. This process increased the buoyancy of the particles. A second channel, 5 mm in diameter and in close proximity to the first, was connected to a peristaltic pump that introduced pulses of water at a rate of approximately 5/s to produce a cyclic motion throughout the soft gelatin. These pulses gave the strong clutter signals necessary to test filter performance, as we show in the next section. Time-varying pressure from the pulsed channel provided an echo-signal component that simulated clutter from extravascular tissues and modulated the steady flow in the first channel.

We found it difficult to produce a significant moving-clutter signal with a single pulsed-channel phantom without also aliasing flow velocities. The challenge is to generate a durable phantom material that will transmit the mechanical energy of pulsed flow deep into the surrounding gelatin, is soft enough to produce a clutter spectrum that overlaps the flow spectrum and allows the echo signal to recombine after each pressure-pulse cycle. Body tissues naturally have these properties because of a heterogeneous layered structure. The two flow-channel phantom design described above gave a clutter signal that periodically shifted scatterers in the ROI without significant strain. Unfortunately, the flow channels in the soft gelatin ruptured regularly. For the second experimental series, we changed to a *slurry* phantom material [28] in place of the solid gelatin for the CF experiments and used long-thin latex balloons with approximately 0.5-mm wall thickness for the two flow channels. The slurry is the same congealed graphite-gelatin as in the solid phantom. Pieces were placed in a blender with a water-propanol solution until slurry particles less than 2 mm in size were produced. The slurry was degassed and allowed to settle in the water-alcohol solution into which the latex flow channels were placed with the geometry of Fig. 4. The settled slurry was very soft, had tissue-like acoustic properties, seemed to transmit mechanical energy with high displacement amplitude, and yet exhibited scatterer motion that allowed echoes to recombine with each pressure pulse.

B. Modeling Pulsatile Wall Motion

To help us design phantom experiments and then translate those results to measurements in the body, we estimated the fluid velocity-vector components of oscillatory flow from equations that model viscous flow in a thin-walled elastic tube [29]. The axial $u(r, x, t)$ and radial $v(r, x, t)$ components of fluid velocity are given by (9) in the Appendix as a function of radial distance r from the tube center, axial distance x from the tube entrance, and time t . The axial velocity located at the center of tube entrance is $u(0, 0, t)$, and $v(a, 0, t)$ is the radial velocity at the channel wall. Their maximum values are plotted in Fig. 5 as a function of the pulsed-pressure frequency parameter Ω . For comparison, the maximum axial velocities for Newtonian Poiseuille flow and pulsatile flow in a rigid tube are shown at the same pressure gradient $k_s = dp/dx$. Model parameters were set to the phantom experiment. The fluid

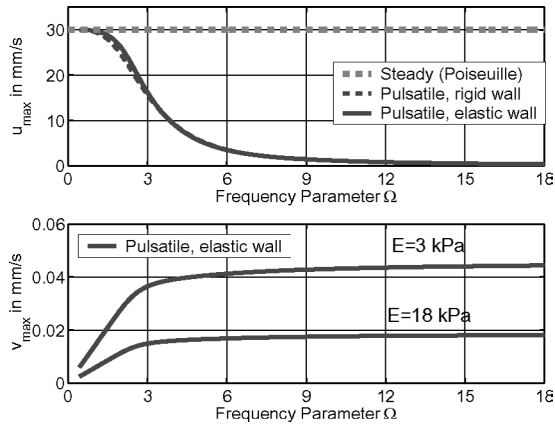


Fig. 5. Computed maximum axial fluid and radial wall velocities in an elastic tube (radius $a = 3$ mm, $h/a = 0.1$, $\nu = 0.5$) for a frequency-independent pressure gradient $k_s = -13.3$ N/(m²·m) as a function of the frequency parameter Ω and elastic modulus E . See the Appendix.

density $\rho = 10^3$ kg/m³ and viscosity $\mu = 0.001$ kg/m·s values are for water. The wall density $\rho_w = 1060$ kg/m³ was that of the gelatin phantom material.

To match our experiment, the pressure pulse frequency was set to the fundamental frequency of 5 Hz ($\Omega = 16.82$) and an elastic modulus of the wall material of $E = 18$ kPa was chosen. The pressure gradient was -13.3 N/(m²·m) to produce a maximum flow velocity of 30 mm/s in the center of the tube at 0 Hz, which corresponds to a mean flow velocity of 15 mm/s for laminar flow. For exact comparisons between predicted and measured values a Fourier decomposition of the pressure pulse used in the experiment is necessary. To calculate flow and wall velocities, solutions for each individual oscillatory pressure component must be derived from (9) and superimposed with one another with correct phases. The inertia of blood or water delays the temporal velocity relative to the pressure as a function of frequency. However, the analysis of the applied pressure pulse shows that the second and third harmonics contain only 5.49% and 0.18% of the total pulse energy. Thus, the wall velocity is mostly determined by the first harmonic component, and investigation of the fundamental provides sufficient accuracy for our application. Fig. 5 clearly shows that increasing Ω slows the fluid velocity and increases the clutter-generating wall velocities—the situation we seek for testing filter performance. However, the maximum radial wall velocity can only reach 4.2% of the axial center velocity of the fluid (water) at this pulse-pressure frequency of 5 Hz. The viscosity of blood increases to $\mu = 0.004$ kg/m·s, and with a cardiac pulse frequency of 1 Hz ($\Omega = 3.76$), the equations predict a peak wall velocity that is just 0.6% of the peak fluid velocity.

C. Color M-Mode

Echo data were acquired in M-mode from the solid phantom above the center of the 3-mm-diameter channel as shown in Fig. 4. We used a single-element, 12.7-

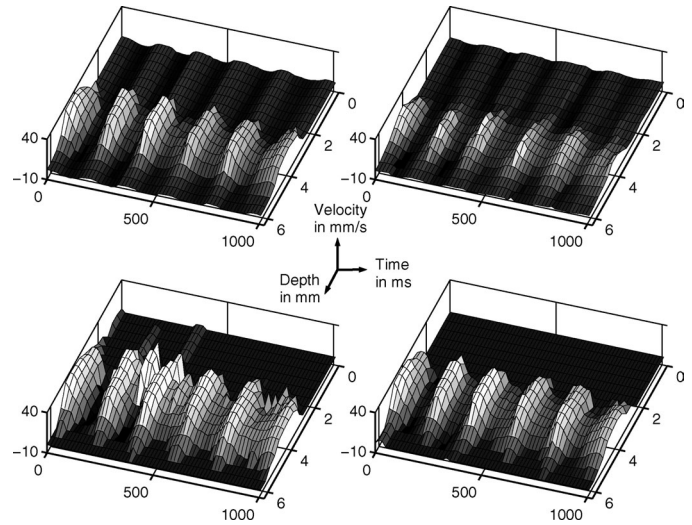


Fig. 6. Different filters were applied to suppress tissue motion: zero-initialized second-order IIR (top left), step-initialized second-order IIR (top right), first-order regression (bottom left), and first-order eigenfilter (bottom right).

mm-diameter, $f/3.5$ spherically focused, 15-MHz transducer. Fig. 12 displays the resulting color M-mode image: color-coded velocities calculated by the 2-D autocorrelator are overlaid on the gray-scale brightness trace. The Gaussian-shaped pulse length was 0.4 mm at -20 dB pulse duration, and the range gate length was set at the same value. Nonoverlapping range gates were used, therefore the vertical color pixel size is 0.4 mm.

Switching off the pulsed-pressure channel, the phantom was motionless and the flow in the 3-mm channel was steady over time giving flow velocities in the range $0 \leq v_z \leq 17$ mm/s. Switching on the pulsed-pressure channel, gelatin (clutter) velocities ranged between ± 5 mm/s, and flow velocities were temporally modulated over the range $-1 \leq v_z \leq 30$ mm/s. The clutter filter should eliminate CF signals outside the flow channel without affecting flow in the channel; that is, the temporal flow modulation should remain.

Fig. 6 shows velocity maps corresponding to the color-flow image of Fig. 12 after four different clutter filters were applied. The zero-initialized IIR filter is unable to suppress the gelatin motion. Step initialization is more efficient at suppressing clutter but also suppresses flow. The regression filter significantly cancels clutter but disturbs the flow profile. Only the eigenfilter completely eliminates clutter without disturbing flow velocities.

Eigenfilters adapt to the statistics of high-energy clutter regardless of the specific frequency characteristics. The FIR and IIR clutter filters require blood and clutter spectra to be separable and also that we know *a priori* which is higher. Polynomial regression filters can successfully filter clutter if the polynomial terms that best model clutter can be found. Eigenfilters adapt naturally. If the eigencomponents can be associated with whatever physical processes are generating the Doppler spectrum, the processes can be

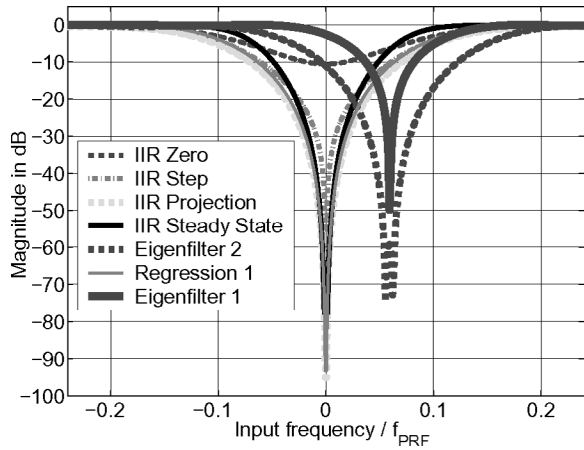


Fig. 7. Filter frequency responses in the range of $-0.25f_{\text{PRF}}$ to $+0.25f_{\text{PRF}}$ for $N = 8$. The second-order IIR Chebyshev filters are highpass with a cut-off frequency of $0.0755f_{\text{PRF}}$ Hz. The eigenfilter was designed to suppress clutter centered at $+0.0566f_{\text{PRF}}$. Increasing the order of the eigenfilter also increases attenuation but widens the stopband.

separated. This feature makes eigenfilters well suited for SF imaging.

D. Color Flow Images

Another advantage of eigenfilters is that asymmetric frequency responses can be easily realized. Traditional filters are most often designed with real coefficients and thus respond symmetrically. Examples of both are shown in Fig. 7. An asymmetrical frequency response is an advantage in CF imaging when the clutter and blood velocities are of equal magnitude but opposite direction. Eigenfilters easily adapt to these situations.

The advantage was demonstrated experimentally by producing Doppler shifts from clutter and blood flow with similar magnitudes but opposite signs. The slurry phantom was ideal for this demonstration. Data were acquired with our lab scanner in a repetitive (gated) acquisition mode. An optical sensor mounted on the peristaltic pump enabled us to adjust the temporal phase of the ultrasonic pulse transmission with respect to the pressure pulse in a manner similar to physiological gating. Thus the 2-D CF images of Fig. 13 and 14 were obtained. Data were recorded during the pressure pulse phase that produced clutter and flow with equal Doppler shift magnitudes but opposite signs, coded as red and blue, respectively. Fig. 13 compares unfiltered CF images with those filtered by a second-order projection-initialization IIR filter with various cut-off frequencies. As the cut-off frequency increases, clutter and flow are both suppressed due to the symmetric frequency response. Fig. 14 shows results for the same data after applying the polynomial regression filter and eigenfilter. Eigenfilter performance is superior for separating signal components with minimal passband distortion.

The B-mode component of these images is distorted because of echo amplitude saturation. The bit depth for Doppler estimation was maximized at the expense of the

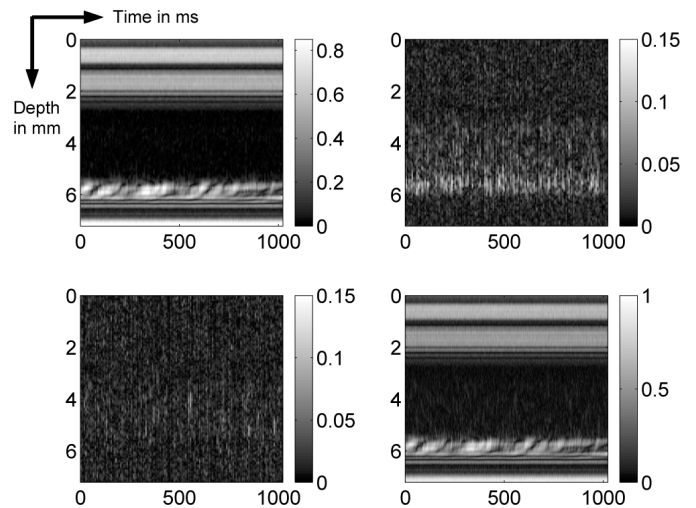


Fig. 8. Separate eigencomponents are shown in an M-mode format when the clutter is from stationary scatterers. In the top row are the brightness eigenimages related to the first (left) and second (right) eigencomponent. The bottom row shows the 3rd eigencomponent (left) followed by the combination of all eight (right). Note the different brightness scalings. Virtually all of the clutter signal is contained in the first eigenimage, and most of the steady-flow signal energy is found in the second eigenimage.

high amplitude graphite-gelatin echoes. B-mode distortion is eliminated by increasing the analog-to-digital converter bit depth.

E. Eigenimages

The spatial distribution of echo energy into various eigencomponents is shown in Fig. 8 for stationary clutter and Fig. 9 for moving clutter. Eigenimages were computed from echo data acquired in the experiment shown in Figs. 4 and 12 and normalized to the highest echo amplitude. Without pulsatility, the phantom echo signal generates a stationary clutter contained almost entirely within the first eigencomponent. With pulsatility, energy of the moving clutter signal extends to the first two eigencomponents. The bright irregular echoes at the bottom of the flow channel are from cornstarch particles that have settled out of suspension.

Eigenimages of these M-mode data are computed as follows: $N = 8$ consecutive echoes with a 1 ms slow-time sampling interval ($\text{PRF} = 1 \text{ kHz}$) are decomposed into 8 eigencomponents by subtracting certain eigencomponents using the eigenfilter approach. Repeating the decomposition for all $1024/8 = 128$ pulse packets gives the eigenimages shown. Each pulse packet is then used to form $N - 1$ echo signal pairs for flow and strain estimation resulting in CF and strain images with 128 columns. Individual estimation of the eigencomponents for every final image column may not be necessary if the clutter movement is uniform. In this case the $N \times N$ autocovariance matrix, estimated by averaging over depth, does not differ significantly as a function of time or image position. However, for more complex imaging environments with nonuniform lateral displace-

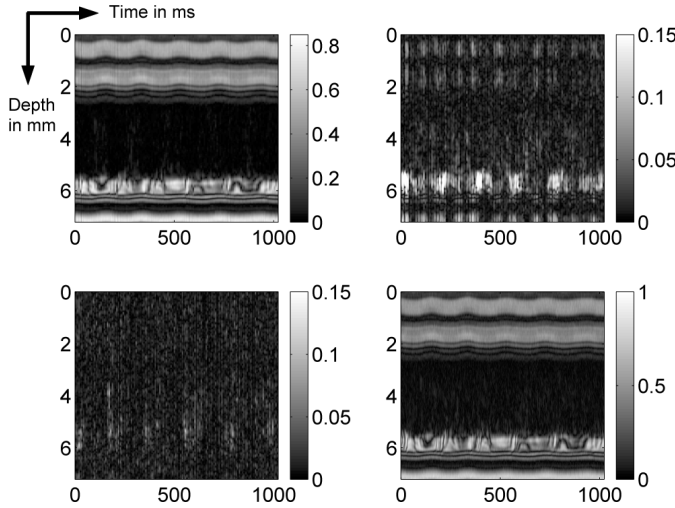


Fig. 9. Separate eigencomponents are shown in an M-mode format when the clutter is from moving scatterers. In the top row are the brightness eigenimages related to the first (left) and second (right) eigencomponent. The bottom row shows the 3rd eigencomponent (left) followed by the combination of all eight (right). Note the different brightness scalings. Clutter is contained in the first two eigenimages.

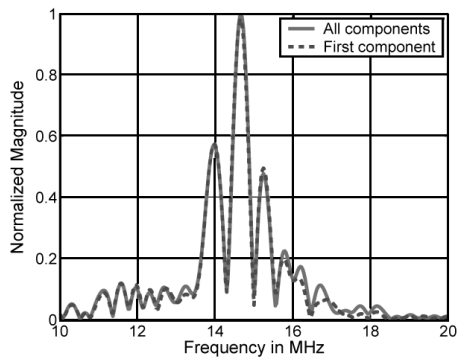


Fig. 10. Fast-time spectra of the clutter component computed from a single pulse packet in the upper part of Fig. 9: all 8 eigencomponents (no filtering) and the first eigencomponent only.

ment gradients, individual decomposition at every LOS is crucial for good filter performance.

F. Strain Images

The precision of correlation-based strain estimates increases with echo signal bandwidth. Fig. 10 shows that the *fast-time* signal bandwidth of the first eigencomponent is essentially the same as of all eight components. Consequently, strain estimates from eigenfiltered echoes are only negligibly degraded in realistic situations.

Fig. 11 shows displacement images for several situations. The axial image resolution is 0.2 mm resulting from a correlation window length of 0.4 mm and a window overlap of 0.2 mm. Strain images are not shown for this data because the axial displacement is virtually constant; therefore, axial strain is zero.

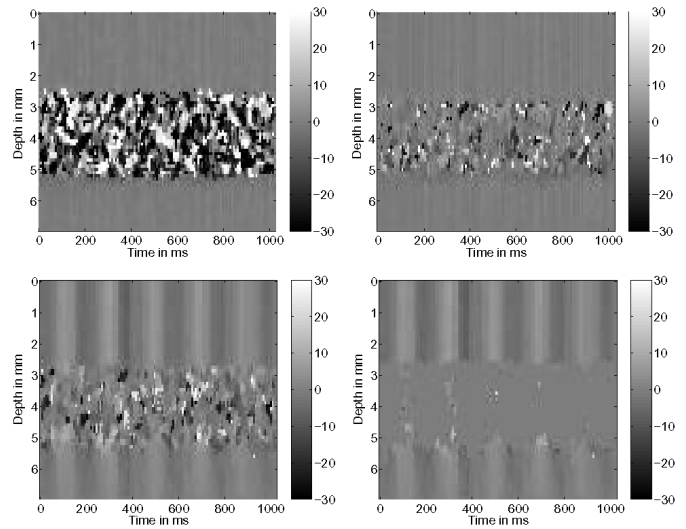


Fig. 11. Displacement images of M-mode data. Top row are for stationary clutter and bottom row for moving clutter. Top left is unfiltered, while the remaining images are filtered using a first-order eigenfilter. These images demonstrate that tissue motion can be estimated independent of flow. The colorbar is scaled in microns.

The top left image in Fig. 11 shows unfiltered displacement estimates of the phantom flow channel when there is no pulsatile flow. Fluid flow minimizes the interframe correlation coefficient between echoes in the channel, which gives the intense decorrelation noise. The upper right image is displacement computed from the same echo data but using only the first eigencomponent. Decorrelation noise is reduced by eliminating much of the flow- and noise-component signal energy. The lower left image of Fig. 11 is the same processing as the upper right except the pulse-flow channel is switched on. Finally, masking all the pixels marked for flow velocity estimation by the first-order eigenfilter, we find the image in the lower right.

G. Toward Strain-Flow Imaging

A CF image using only the first eigencomponents and the corresponding displacement-flow image are shown in Fig. 15. This image pair clearly shows how well the moving clutter signal is separated from the flow and how information about blood and tissue motion can be merged. Unfortunately, the nature of the pulse-phantom stimulus gave constant displacement, and zero axial strain results.

The final experiment was recorded using a commercial system (Siemens Elegra) modified to acquire IQ data. Data acquisition on the Elegra is described in [5]. The unknown wall-filtering of the CF system was not harmful in this situation because the only movement came from constant channel flow. Strain was computed from two data frames acquired after external compression from a plate in which the linear array was mounted. The static strain image was fused with the system's CF image (Fig. 16). This result demonstrates that SF imaging on commercial systems is possible. However, for more challenging exper-

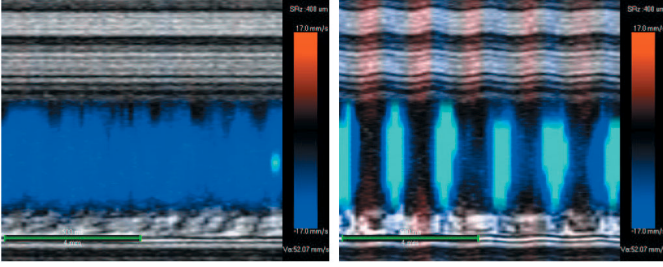


Fig. 12. Left: Color M-mode image shows steady flow in the 3-mm-diameter flow channel away from the transducer with the pulse channel off. Right: Color M-mode image of the same channel temporally modulated by the adjacent pulsed-pressure channel. The color scales of both images are the same. Cyan regions indicate velocities away from the transducer that are out of range. Clutter appears as color outside the channel.

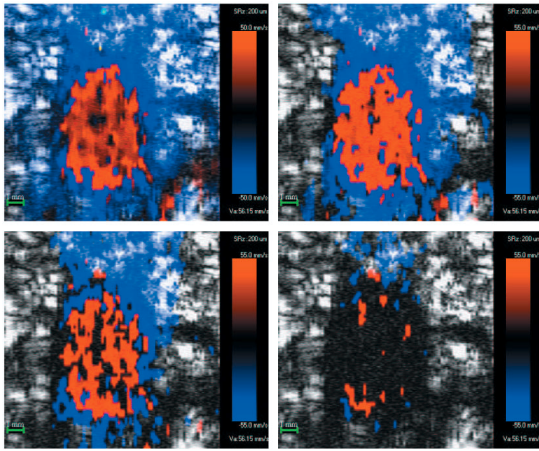


Fig. 13. 2-D CF images where the flow and clutter Doppler shifts are equal in magnitude and opposite in sign. Unfiltered (upper left) and second-order projection-initialized IIR filter with 3 increasing cut-off frequencies (highest value lower right) and $N = 8$. The length of the green bars in the lower left corners represents 1 mm.

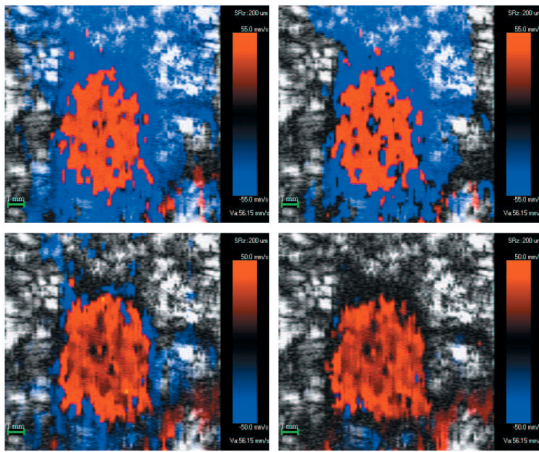


Fig. 14. 2-D CF images for first-order (upper left) and second-order (upper right) polynomial regression filters. In the bottom row are the results for a first-order (lower left) and second-order (lower right) eigenfilter with $N = 8$. The length of the green bars in the lower left corners represents 1 mm.

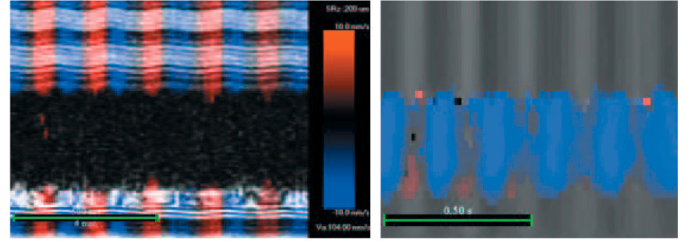


Fig. 15. Left: CF image where only the first eigencomponents are used to estimate velocity from the 2-D autocorrelator. Right: Corresponding displacement-flow image where displacement is computed from the first eigencomponent only. Flow is derived from all but the first eigencomponent. The length of the green bars in the lower left corners represents 500 ms (horizontally) and 4 mm (vertically).

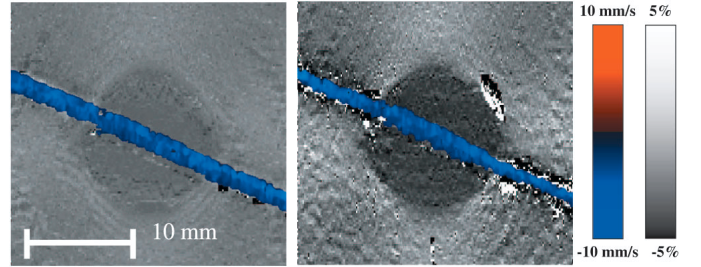


Fig. 16. Merged strain and color-flow data obtained from the complex baseband signals of a Siemens Elegra system at 7.5 MHz. External compression of 1% (left) and 3% (right) of the phantom height was applied. The velocity of the steady flow was about 8 mm/s. As the inclusion in the middle was stiffer, the flow channel collapsed less than within the outer softer regions. As a result, the flow velocity was slightly increased in the softer regions. This effect can be seen more clearly at higher compressions (right).

imental strain-flow situations, access to echo data pulse packets before wall filtering is necessary.

VII. CONCLUSIONS

A method for estimating flow velocities and tissue strain independently from a single set of echo data was described. Eigenfilters provide a clear separation between signal energy from these two components of motion that is adaptable to a wide range of imaging conditions. These phantom studies suggest that strain-flow imaging is possible *in vivo* for vascular imaging.

APPENDIX A

After elastic wall and Navier–Stokes fluid motion equations have been coupled and matched at the neutral position $r = a$ of the tube wall, the following expressions for the axial and radial velocities can be found [29]

$$\begin{aligned} u(r, x, t) &= \frac{k_s a^2}{\mu \Lambda^2} \left[1 - G \frac{J_0(\zeta)}{J_0(\Lambda)} \right] e^{j\omega(t - \frac{x}{c_p})} \\ v(r, x, t) &= \frac{-k_s}{2\rho c_p} \left[\frac{r}{a} - G \frac{2J_1(\zeta)}{\Lambda J_0(\Lambda)} \right] e^{j\omega(t - \frac{x}{c_p})} \end{aligned} \quad (9)$$

where G is referred to as the “elasticity factor” given by

$$G = \frac{2 + z(2\nu - 1)}{z(2\nu - g)}, \quad (10)$$

and

$$\Omega = \sqrt{\frac{\rho\omega}{\mu}}a; \Lambda = j^{3/2}\Omega; \zeta = \Lambda \frac{r}{a}; g = \frac{2J_1(\Lambda)}{\Lambda J_0(\Lambda)}; z = \frac{E\nu h}{\rho a c_p^2}.$$

The angular frequency is ω , J_0 and J_1 are Bessel functions of zero and first order, $E\nu = E/(1-\nu^2)$ where ν represents Poisson’s ratio, $j = \sqrt{-1}$, $k_s = dp/dx$ is the longitudinal pressure gradient, and ρ and μ are density and viscosity.

It can be seen from the above equations that the pulse wave velocity (PWV) c_p must be known to calculate z and thereafter G to find the axial and radial velocities. The well-known Moens–Korteweg PWV expression is defined for nonviscous, pulsatile fluid of constant density flowing in a thin-walled elastic tube ($h \ll d$):

$$c_0 = \sqrt{\frac{Eh}{\rho d}}.$$

However, if fluid viscosity needs to be included, the solution for the PWV is more complicated but can be obtained from z after solving the following quadratic equation [29]:

$$\begin{aligned} [(g-1)(\nu^2-1)]z^2 + \left[\frac{\rho_w h}{\rho a}(g-1) + (2\nu-0.5)g - 2 \right] z \\ + \frac{2\rho_w h}{\rho a} + g = 0, \end{aligned} \quad (11)$$

where ρ_w is the density of the wall material, and z as a measure of the PWV in viscous flow is a complex number. Therefore, the PWV is also complex and shows dispersion because the solution for z is frequency-dependent. For viscous fluid, c_p is related to c_0 as follows:

$$c_p = \sqrt{\frac{2}{z(1-\nu^2)}} c_0. \quad (12)$$

The wave propagation velocity can be found from the real part of c_p , and the wave attenuation is determined by its imaginary part. The PWV variation with angular frequency ω , and kinematic viscosity $\nu = \mu/\rho$ can be expressed as a function of a single, nondimensional frequency parameter $\Omega = a\sqrt{\omega/\nu}$. We also correct c_0 by taking tube tethering, finite wall thickness h and Poisson’s ratio ν of the wall into account [30]. This becomes necessary, especially *in vivo*, because the classical model assumes that no longitudinal stresses are applied, i.e., the free tube will shorten longitudinally when it is extended radially. Arteries, however, are anatomically attached to their surroundings. The walls are stiffly tethered by a longitudinal elastic constraint such that they are unable to move longitudinally under the influence of the viscous drag from the blood flow. In this case, radial stretch induces longitudinal tension, which, in turn, increases the PWV. Furthermore,

the influence of wall viscosity is very similar to that of tethering because internal viscosity impedes the longitudinal movement of the wall [31]. Of course, now the incremental elastic wall modulus becomes a complex number, indicating that radius changes always lag behind pressure changes. It is known that for a Poisson’s ratio close to 0.5, which is the case for soft tissue, c_p increases by no more than 16% compared with c_0 [32].

ACKNOWLEDGMENTS

The authors would like to thank Prof. Mair Zamir (Department of Applied Mathematics, University of Western Ontario, Canada) for providing email support regarding pulsatile fluid and wall motion modelling.

We would also like to thank Ms. Samantha Nicholson for the final proofreading of the manuscript.

REFERENCES

- [1] S. I. Rabben, S. Bjærum, V. Sørhus, and H. Torp, “Ultrasound-based vessel wall tracking: An auto-correlation technique with RF frequency estimation,” *Ultrasound Med. Biol.*, vol. 28, pp. 507–517, 2002.
- [2] M. O’Donnell, A. R. Skovoroda, B. Shapo, and S. Emelianov, “Internal displacement and strain imaging using ultrasonic speckle tracking,” *IEEE Trans. Ultrason., Ferroelect., Freq. Contr.*, vol. 41, pp. 314–325, 1994.
- [3] P. Chaturvedi, M. F. Insana, and T. J. Hall, “Testing the limitations of 2-D local companding in strain imaging using phantoms,” *IEEE Trans. Ultrason., Ferroelect., Freq. Contr.*, vol. 45, pp. 1022–1031, 1998.
- [4] A. P. G. Hoeks, P. J. Brands, J. M. Willigers, and R. S. Reneman, “Non-invasive measurement of mechanical properties of arteries in health and disease,” *Proc. Instrn. Mech. Engrs.*, vol. 213, pp. 195–202, 1999.
- [5] J. J. Mai and M. F. Insana, “Strain imaging of internal deformation,” *Ultrasound Med. Biol.*, vol. 28, pp. 1475–1484, 2002.
- [6] R. H. Fletcher and D. W. Burlage, “An initialization technique for improved MTI performance in phased array radars,” *Proc. IEEE*, vol. 60, pp. 1551–1552, 1972.
- [7] E. S. Chornoboy, “Initialization for improved IIR filter performance,” *IEEE Trans. Signal Processing*, vol. 40, no. 3, pp. 543–550, 1992.
- [8] A. P. Kadi and T. Loupas, “On the performance of regression and step-initialized IIR clutter filters for color Doppler systems in diagnostic medical ultrasound,” *IEEE Trans. Ultrason., Ferroelect., Freq. Contr.*, vol. 42, no. 5, pp. 927–937, 1995.
- [9] T. Hasebe, K. Mukai, H. Tsuda, and A. Ochiai, “New prognostic histological parameter of invasive ductal carcinoma of the breast,” *Path. Int.*, vol. 50, pp. 263–272, 2000.
- [10] R. A. Walker, “The complexities of breast cancer desmoplasia,” *Breast Cancer Res.*, vol. 3, pp. 143–145, 2001.
- [11] N. Weidner, J. Folkman, F. Pozza, P. Bevilacqua, E. N. Allred, D. H. Moore, S. Meli, and G. Gasparini, “Tumor angiogenesis: A new significant and independent prognostic indicator in early-stage breast carcinoma,” *J. Natl. Cancer Inst.*, vol. 84, pp. 1875–1887, 1992.
- [12] Ch. Kargel, G. Höbenreich, G. Plevnik, B. Trummer, and M. F. Insana, “Velocity estimation and adaptive clutter rejection filtering for color flow imaging,” in *Proc. WSEAS Conf. Sig. Speech Image Proc.*, 2002.
- [13] Ch. Kargel, G. Plevnik, B. Trummer, and M. F. Insana, “Ultrasonic visualization of tumor blood flow,” *IEEE Trans. Instrum. Meas.*, submitted for publication.
- [14] S. Bjærum, H. Torp, and K. Kristoffersen, “Clutter filters adapted to tissue motion in ultrasound color flow imaging,” *IEEE Trans. Ultrason., Ferroelect., Freq. Contr.*, vol. 49, no. 6, pp. 693–704, 2002.

- [15] T. Loupas, R. B. Peterson, and R. W. Gill, "Experimental evaluation of velocity and power estimation for ultrasound blood flow imaging by means of a two-dimensional autocorrelation approach," *IEEE Trans. Ultrason., Ferroelect., Freq. Contr.*, vol. 42, no. 4, pp. 689–699, 1995.
- [16] C. Kasai, K. Namekawa, A. Koyano, and R. Omoto, "Real-time two-dimensional blood flow imaging using an autocorrelation technique," *IEEE Trans. Sonics Ultrason.*, vol. SU-32, no. 3, pp. 458–464, 1985.
- [17] W. D. Barber, J. W. Eberhard, and S. G. Karr, "A new time domain technique for velocity measurements using Doppler ultrasound," *IEEE Trans. Biomed. Eng.*, vol. BME-32, pp. 213–229, 1985.
- [18] M. F. Insana, L. T. Cook, M. Bilgen, P. Chaturvedi, and Y. Zhu, "Maximum likelihood approach to strain imaging using ultrasound," *J. Acoust. Soc. Amer.*, vol. 107, pp. 1421–1434, 2000.
- [19] N. R. Nightingale, M. L. Palmeri, R. W. Nightingale, and G. E. Trahey, "On the feasibility of remote palpation using acoustic radiation force," *J. Acoust. Soc. Amer.*, vol. 110, pp. 625–634, 2001.
- [20] Ch. Kargel, "Hybrid optical and digital signal processing in a laser speckle measurement technique," Ph.D. dissertation, Graz University of Technology, Graz, Austria, 1999.
- [21] A. V. Oppenheim and R. W. Schaffer, *Discrete Time Signal Processing*. 2nd ed. Englewood Cliffs, NJ: Prentice-Hall, 1999.
- [22] H. Torp, "Clutter rejection filters in color flow imaging: A theoretical approach," *IEEE Trans. Ultrason., Ferroelect., Freq. Contr.*, vol. 44, no. 2, 1997.
- [23] S. Bjærum, H. Torp, and K. Kristoffersen, "Clutter filter design for ultrasound color flow imaging," *IEEE Trans. Ultrason., Ferroelect., Freq. Contr.*, vol. 49, no. 2, 2002.
- [24] R. C. Gonzalez and R. E. Woods, *Digital Image Processing*. Reading, MA: Addison-Wesley, 1992, p. 157.
- [25] G. Höbenreich, "Performance evaluation of adaptive clutter rejection filters for blood flow imaging," Masters thesis, Graz University of Technology, Graz, Austria, 2002.
- [26] Ch. Kargel, B. Trummer, G. Plevnik, C. Pellet-Barakat, J. J. Mai, and M. F. Insana, "Is ultrasonic imaging a sensitive indicator of spatially varying elastic anisotropy?," in *Proc. IEEE Ultrason. Symp.*, vol. 01CH37263, 2001, pp. 1659–1662.
- [27] E. L. Madsen, J. A. Zagzebski, R. A. Banjavic, and R. E. Jutila, "Tissue mimicking materials for ultrasound phantoms," *Med. Phys.*, vol. 5, pp. 391–394, 1978.
- [28] T. J. Hall, M. F. Insana, N. M. Soller, and L. A. Harrison, "Ultrasound contrast-detail analysis: A preliminary study in human observer performance," *Med. Phys.*, vol. 20, pp. 117–127, 1993.
- [29] M. Zamir, *The Physics of Pulsatile Flow*. New York: Springer Verlag, 2000.
- [30] D. H. Bergel, "The dynamic elastic properties of the arterial wall," *J. Physiol.*, vol. 156, pp. 458–469, 1961.
- [31] M. G. Taylor, "An experimental determination of the propagation of fluid oscillations in a tube with visco-elastic wall; together with an analysis of the characteristics required in an electrical analogue," *Phys. Med. Biol.*, vol. 4, pp. 63–82, 1959.
- [32] D. A. McDonald, *Blood Flow in Arteries*. 2nd ed. Southampton: Camelot Press Ltd., 1974.



Christian Kargel (S'97–A'99) graduated from the the Graz University of Technology in Austria with a B.S. and M.S. degree in electrical engineering (electronics and communications) with honors. In 1995 he joined the Department of Electrical Engineering at the Graz University of Technology and completed his Ph.D. degree with honors in coherent optics and statistical signal processing in April 1999. Until August 2000 Christian was assistant professor of electrical measurement, measurement signal processing and instrumentation

at the Graz University of Technology. From September 2000 to July 2002, he was a visiting assistant professor in the Department of

Biomedical Engineering at the University of California, Davis, where his research work was focused mainly on ultrasound-based velocity estimation and strain imaging. Since October 2002, Dr. Kargel has been a professor of Medical Electronics and Instrumentation in the newly created Department of Medical Information Technology at the Carinthia Tech Institute, University of Applied Sciences, Austria.

His research interests include medical imaging, electronics, and instrumentation as well as biomedical signal and optical information processing. He is a member of IEEE and SPIE.



Gernot Höbenreich was born in Graz, Austria, on October, 1976. He completed his undergraduate studies in electrical engineering and recently received his Dipl.-Ing. degree in biomedical engineering from the Graz University of Technology, Austria. He worked for eight months at the Department of Biomedical Engineering at the University of California, Davis, as a research assistant. His work focused on clutter rejection filtering for color flow imaging. His research interests include digital signal processing and its applications

to medical imaging as well as software development for medical applications.



Birgit Trummer was born in Graz, Austria, in 1971. She received the Dipl.-Ing. degree in electrical engineering (process design) from the Graz University of Technology in 2001. Her thesis was on contactless displacement-measurement using laser speckles. From 2001 to 2002 she was a postgraduate researcher at the Biomedical Engineering Department of the University of California, Davis, where she worked on the development of an experimental ultrasonic scanner system. Her main field of interest is digital signal processing.



Michael F. Insana (M'85) received his Ph.D. in medical physics from the University of Wisconsin, Madison, in 1983. His dissertation topic was acoustic scattering and absorption in biological tissues. He was a research physicist at the FDA from 1984 to 1987, where he developed methods for describing tissue microstructure from the statistical properties of echo signals. From 1987 to 1999, he was with the Department of Radiology at the University of Kansas Medical Center. There, he directed an imaging research lab that designed

and evaluated new ultrasonic imaging methods for studying progressive renal failure and breast cancer. Since 1999, Mike has been Professor of Biomedical Engineering at the University of California, Davis. He is vice chair of the department and chair of the graduate group. His research is the development of novel ultrasonic instrumentation and methods for imaging soft tissue microstructure, elasticity, and blood flow. The goal is to understand basic mechanisms of tumor formation and responses to therapy. His research includes the fundamentals of imaging system design and performance evaluation, signal processing, detection, and estimation. He is a member of the IEEE and ASA, Fellow of the Institute of Physics, and Associate Editor for *IEEE Transactions on Medical Imaging*.